Hysteresis Bearingless Slice Motors with Homopolar Flux-biasing

Hysteresis Bearingless Slice Motors with Homopolar Flux-biasing

Minkyun Noh, Wolfgang Gruber, *Member, IEEE,* and David L. Trumper, *Member, IEEE*

***Abstract*—We present a new concept of bearingless slice motor that levitates and rotates a ring-shaped solid rotor. The rotor is made of a semi-hard magnetic material exhibiting magnetic hysteresis, such as D2 steel. The rotor is radially biased with a homopolar permanent-magnetic flux, on which the stator can superimpose 2-pole flux to generate suspension forces. By regulating the suspension forces based on position feedback, the two radial rotor degrees of freedom are actively stabilized. The two tilting degrees of freedom and the axial translation are passively stable due to the reluctance forces from the bias flux. In addition, the stator can generate a torque by superimposing 6-pole rotating flux, which drags the rotor via hysteresis coupling. This 6-pole flux does not generate radial forces in conjunction with the homopolar flux or 2-pole flux, and therefore the suspension force generation is in principle decoupled from the driving torque generation. We have developed a prototype system as a proof of concept. The stator has twelve teeth, each of which has a single phase winding that is individually driven by a linear transconductance power amplifier. The system has four reflective-type optical sensors to differentially measure the two radial degrees of freedom of the rotor. The suspension control loop is implemented such that the phase margin is 25 degrees at the cross-over frequency of 110 Hz. The prototype system can levitate the rotor and drive it up to about 1730 rpm. The maximum driving torque is about 2.7 mNm.**

***Index Terms*—Hysteresis motors, bearingless motors, flux-biasing, magnetic bearings, slice motors.**

I. Introduction

BEARINGLESS motors, or self-bearing motors, are special types of electric machines that can levitate and drive a rotor with a single stator unit. The stator of bearingless motors can apply not only a driving torque about the rotor rotational axis, but also constraint forces and torques for the other degrees of freedom. This enables elimination of mechanical bearings in a compact form factor. Since 1980s, bearingless motor technology has drawn international research efforts, and therefore led to developments of bearingless motors of various types, including permanent magnet types, induction types, and reluctance types [1].

Some pump applications, such as those for blood or high-purity chemical processes, find bearingless motors especially useful due to their contact- and contamination-free operation. Bearingless slice motors [2], [9], [10] are particularly suitable for these applications: They actively control the axial impeller rotation for a driving torque and the two radial translations for feedback stabilization. The remaining three degrees of freedom are passively stable due to the reluctance forces between the stator teeth and the impeller containing a disk-shaped permanent magnet. The passive stabilization saves the bearingless motors from otherwise required extra components, such as sensors, power amplifiers, and windings. Gruber et al. developed a bearingless slice motor that drives a reluctance rotor [11]. Here, the magnet is eliminated from the rotor and placed on the stator to provide homopolar flux-biasing to the rotor. Such bearingless motors with a magnet-free rotor can save operational costs in applications that require disposable

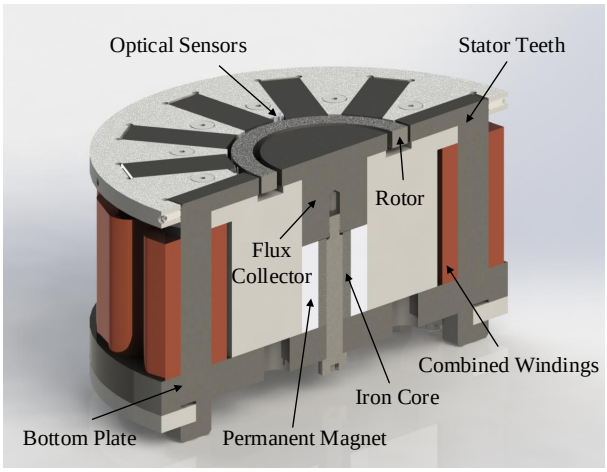

(a)

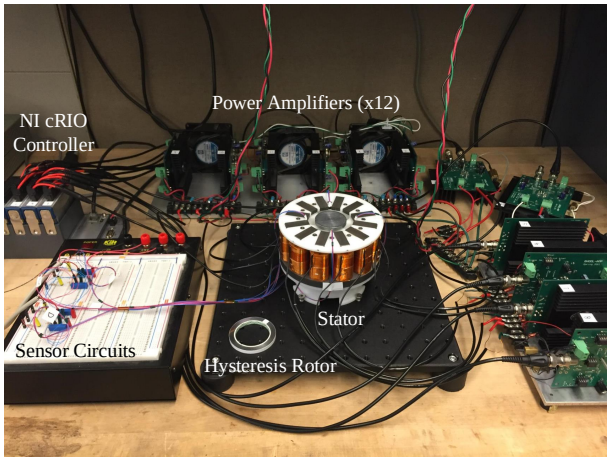

(b)

Fig. 1. (a) 3D rendering of the prototype bearingless motor (cross-sectional side view). (b) Photograph of the prototype system.

M. Noh and D. L. Trumper are with the Department of Mechanical Engineering, Massachusetts Institute of Technology, Cambridge, MA 02139 USA (e-mail: minkyun@mit.edu; trumper@mit.edu)

W. Gruber is with the Institute of Electrical Drives and Power Electronics, Johannes Kepler University, 4040 Linz, Austria (e-mail: wolfgang.gruber@jku.at)

Manuscript received January ?, 2017; revised April ?, 2017.

TABLE I
BEARINGLESS SLICE MOTORS DEVELOPED FOR BLOOD PUMP APPLICATIONS.

Reference	Rotor Type	Rotor Diameter (mm)	Rotor Height (mm)	Rotor Mass (g)	Magnetic Air-gap (mm)	Axial Stiffness (N/mm)	Radial Stiffness (N/mm)	Tilting Stiffness (N/mm)	Force Sensitivity (N/A)	Max. Speed (rpm)	Rated Torque (mNm)
Barletta et al. [2]	PM	45	5	-	3	3.8	-4.6	0.69	3.68	5000	80
Ueno et al. [3]	PM	60	8	90	1	-	-	-	-	9000	-
Schöb et al. [4]	PM	45	5	-	3	3.8	-4.6	0.69	3.68	5000	80
Onuma et al. [5]	PM	53.4	8	70	1	2.5	-31.5	0.57	5.8	2400	30
Asama et al. [6]	PM/Reluctance	50	10	77	0.5	16	-43	3.7	4.3	2000	20
Asama et al. [7]	PM/Reluctance	45	10	110	0.85	7.3	-29	1.7	2.5	4000	22
Onuma et al. [8]	PM	58	8	80	1.5	3.5	-27.5	0.6	9.4	1600	50
Our prototype	Hysteresis	57	5	37	1	1.17	-5.39	0.36	21	1730	2.67

rotor/impeller units.

In this paper, we present a new concept of a bearingless slice motor that drives a ring-shaped hysteresis rotor. Replacing the toothed ring in [11] with an axisymmetric solid ring enables some favorable characteristics. First, the rotor is robust and simple to construct. Second, superimposing 2-pole flux on the homopolar bias flux generates a suspension force that is independent of the rotor angle but only dependent on the direction and magnitude of the 2-pole flux. Third, additional superposition of rotating flux of higher pole numbers, i.e., 6- or 8-pole, can generate a hysteresis torque in such a way that it does not interfere with the suspension force generation. Specifically, the suspension force generation is not affected by the relative angle between the 2-pole flux and the higher-pole flux. Therefore, our bearingless motor is free from angle sensors and does not require the associated commutation algorithm for suspension force generation as well as for torque generation. These characteristics, together with the inherently smooth torque of hysteresis motors, make our new bearingless motor suitable for special applications, such as pumps for blood or other delicate biological samples that require disposable impeller replacement. Table I lists key design parameters and performance values of our prototype system in comparison with the bearingless slice motors developed for blood pumps in the literature. Although our proof-of-concept prototype shows lower torque capability associated with hysteresis motors, the passive stiffnesses and maximum speed are comparable to the prior art.

Bearingless hysteresis motors were first conceptualized and realized by Imani-Nejad [12], and further studied by Zhou [13] in application to a satellite attitude control system. Our bearingless motor newly incorporates homopolar flux-biasing, which enables decoupling the force and torque generations, force generation independent of the rotor position, higher force/current sensitivity for suspension, and suspension force linearization. These benefits originate from the similarity in magnetic structure to flux-biased magnetic bearings [14], [15] and homopolar/hybrid bearingless motors [16].

The operating principle and the design of our bearingless motor have been first introduced in [17] and disclosed in [18]. Our contributions building upon this previous work include: design modification and fabrication of the prototype motor, FEA simulations on the prototype motor, building the control system including sensors and power amplifiers, and hardware testings. The rest of the paper is organized as follows: Section II discusses the operating principle of our bearingless motor. Mechanisms for suspension force and driving torque generation are discussed, followed by the condition under which the two mechanisms can be decoupled. Section III presents a prototype system and discuss the construction details. Section IV shows some testing results on the prototype system, which include the frequency responses of the suspension control as well as torque estimates from the braking time measurements. Section V gives conclusions and suggestions for further work.

II. OPERATING PRINCIPLE

Figure 1 shows the design of our bearingless motor and the prototype system. The stator mainly consists of a bottom plate, twelve stator teeth, twelve combined windings, and a flux biasing structure comprising a permanent magnet and a flux collector. The stator teeth and the flux collector form an annular groove, in which a ring-shaped rotor is inserted. The permanent magnet provides a bias flux through the hysteresis rotor in the radial direction. The level of bias flux can be adjusted with an iron core inserted into the permanent magnet. The ring-shaped rotor is made of D2 steel, which has some favorable characteristics for our design: First, its permeability is relatively high and therefore advantageous to generate reluctance forces. Second, D2 steel exhibits some level of magnetic hysteresis, which can be utilized to generate a hysteresis torque.

The operating principle of a homopolar hysteresis bearingless motor can be best understood as a combination of a flux-biased magnetic bearing [14], [15] and a hysteresis motor [19]. We next discusses the force generation mechanism of a flux-biased magnetic bearing as applied to our bearingless motor design. Following this, we discuss hysteresis torque generation accomplished by superposing an additional 6-pole rotating magnetic flux.

A. Force generation

Figure 2a schematically shows a cross-sectional side view of our bearingless motor. Here, the ring-shaped rotor forms two air-gaps with the stator: an outer air-gap with the stator teeth, and an inner air-gap with the flux collector. The homopolar bias flux (dashed blue lines) from the permanent magnet traverses through the hysteresis rotor radially outwards and returns via the stator bottom plate. As the stator superimposes

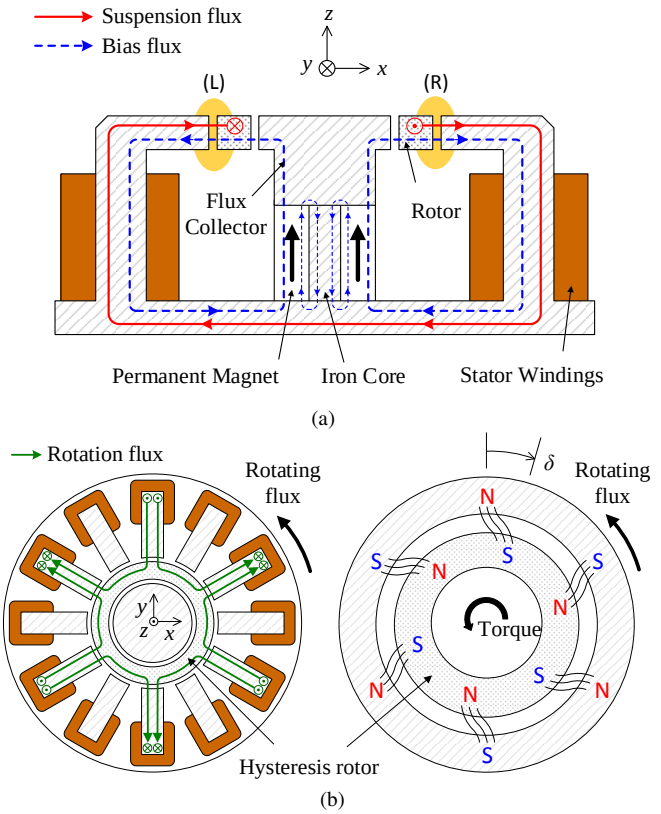

Fig. 2. Schematic diagram of the bearingless motor: (a) Cross-sectional side view illustrating the suspension force generation. The flux density of the air-gap (R) is stronger than that of the air-gap (L), thereby generating a reluctance force to the positive x-direction. (b) Top view illustrating the torque generation. The rotating 6-pole flux drags the rotor via an hysteresis coupling.

2-pole suspension flux (solid red lines), the net flux density in the outer air-gap weakens in area (L) and strengthens in area (R), thereby generating a differential reluctance force on the rotor to the positive x-direction. The direction of the suspension force is determined by the 2-pole flux direction, and the magnitude of the suspension force is determined by the strength of the 2-pole flux. Therefore, by controlling the direction and magnitude of 2-pole suspension flux based on the position measurements, we can actively stabilize the rotor translations in any radial direction. Due to the homopolar bias flux, other degrees of freedom, i.e., translation along the z-axis and tilts about the x- and y-axes, are passively stable. Ignoring the rotor hysteresis in the radial direction, the force generation mechanism is similar to those of flux-biased magnetic bearings [14], [15].

B. Torque generation

Figure 2b illustrates the mechanism of hysteresis torque generation in our design. As the stator imposes 6-pole rotating flux (solid green lines), the rotor becomes magnetized with a rotating 6-pole pattern. The induced magnetization lags behind the stator excitation by some angle δ due to the hysteresis. The interaction between the excitation magnetic fields and the induced magnetization generates a torque

$$\tau = \frac{VP_r}{4\pi} \oint_C B_\theta \, dH_\theta \tag{1}$$

for sufficiently thin-walled rotors [19]. Here, V is the rotor volume, P_r is the pole-number of the rotating excitation fields, H_θ is the tangential component of the magnetic field intensity in the rotor, B_θ is the tangential component of the magnetic flux density in the rotor, and C is the circumferential contour in the thin-walled rotor.

The torque generation mechanism can be implemented in such a way that it does not interfere with the force generation mechanism. This is possible by choosing the pole-number P_r of the rotation flux such that

$$P_r \neq P_b \pm 2 \tag{2}$$

and

$$P_r \neq P_s \pm 2, \tag{3}$$

where $P_b = 0$ is the pole-number of bias flux and $P_s = 2$ is the pole-number of suspension flux. Equations (2) and (3) are based on the $P\pm2$ principle [1], which states that given the flux distribution of pole-number P_1, the necessary and sufficient condition to generate a suspension force is to superimpose additional flux distribution of pole-number $P_2 = P_1 \pm 2$. We consider homopolar bias flux as a flux wave with zero pole number, which enables application of the $P \pm 2$ principle to homopolar-type magnetic bearings and bearingless motors [1, p. 274]. In our design, we choose the rotation flux of pole-number $P_r = 6$ so that it does not generate radial forces by interacting with either of the homopolar bias flux $(P_b = 0)$ and the 2-pole suspension flux of $(P_s = 2)$.

As well, the suspension force generation does not interfere with the torque generation. That is because the homopolar bias flux and the 2-pole suspension flux do not generate a significant drag torque. When the rotor is stabilized at the center under low disturbance force, the variation of the bias flux and suspension flux along the rotor circumference is small, thereby generating negligible hysteresis and eddy-current drags. Thus, the mechanisms for torque generation and suspension force generation are decoupled in principle.

III. Prototype System

We have built a prototype system as shown in Figure 1b. Here, the stator is mounted on an optical breadboard. In the photograph, the rotor is taken out of the stator and placed next to it. Four optical sensors mounted on the stator measure the x- and y-positions of the rotor. The position measurements are sent to the real-time controller, in which the suspension and rotation control algorithms are implemented. The controller sends reference current signals to twelve transconductance power amplifiers, which individually drive the twelve-phase stator windings. The rest of this section discusses each module in more detail.

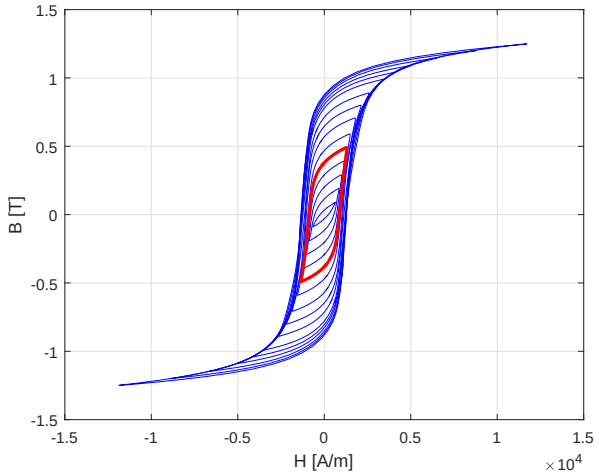

Fig. 3. B-H hysteresis loops of D2 steel measured at 20 Hz following the IEC 60404-6 international standard. The solid red line is for the case where the flux density is sinusoidal with an amplitude of 0.5 T

A. Rotor and stator

The rotor is made from solid D2 steel machined into a ring-shape with 57-mm outer diameter, 45-mm inner diameter, and 5-mm height. D2 steel is a semi-hard magnetic material that exhibits B-H hysteresis as shown in Figure 3. Here, the hysteresis loops are measured from a toroidal D2 steel sample of 55-mm outer diameter, 45-mm inner diameter, and 5-mm height at the excitation frequency of 20 Hz, in accordance with the IEC 60404-6 international standard. The permeability of D2 steel is relatively high ($\mu \approx 300\mu_0$), which is advantageous to generate reluctance forces for magnetic suspension. The aspect ratio (height/diameter) of the rotor is designed relatively small, so as to passively stabilize three rotor degrees of freedom, θ_x, θ_y and z, as in slice motors.

The stator mainly consists of a bottom plate, twelve teeth, twelve single-phase windings, and a flux-biasing structure in the middle. The stator bottom plate and teeth are made with laminated steel sheets of 0.5-mm thickness. The steel sheets are first bonded to form a laminated stack, cut via wire-electrical discharge machining (wire-EDM) into the desired shape, and finally assembled together. Each stator tooth is wound with a short-pitched winding, which is made of 0.5-mm diameter magnet wire of 800 turns. Each phase winding has a series self-inductance of $L_s = 185\,\mathrm{mH}$ and a series resistance of $R_s = 6\,\Omega$ as measured at 20 Hz. The stator has a flux collector and a permanent magnet to provide a bias flux through the hysteresis rotor. The flux collector is made of low-carbon steel. Since the AC stator flux returns through the rotor and does not penetrate into the flux collector, lamination is not necessary for this part. We use a NeFeB permanent magnet of 25.4-mm outer diameter, 12.7-mm inner diameter, and 25.4-mm height. The level of bias flux can be adjusted by inserting an iron core into the permanent magnet as illustrated in Figure 2a. The iron core provides a parallel return path for the permanent-magnetic bias flux, thereby decreasing the portion of bias flux through the air-gap. Currently, an iron core made of low-carbon steel (12.6-mm outer diameter, 6.5-mm inner diameter, 25.4-mm height) is inserted, which leads to the bias flux density in the outer air-gap of $B_{bias} = 0.13\,\mathrm{T}$ as measured. This bias flux density is sufficient to passively levitate the rotor with mass $m = 37\,\mathrm{g}$ in the z-direction. The axial sag of the rotor from the stator top surface is $\delta z \approx 0.3\,\mathrm{mm}$. Larger bias flux improves the passive stiffness, but also makes the suspension control loop design more challenging as it increases the magnitude of open-loop negative radial stiffness as well. Key design parameters of the rotor and stator are summarized in Table II.

We have performed magnetostatic ANSYS Maxwell simulations to predict the performance. The hysteresis of D2 steel is not accounted for in the simulation. Instead, the normal magnetization curve, a single-valued curve connecting the tips of minor hysteresis loops, is obtained from the measured data and used for the simulation. The simulation results predict that the rotor axial stiffness is $k_z = 1.17\,\mathrm{N/mm}$, open-loop radial stiffness is $k_r = -5.39\,\mathrm{N/mm}$, and tilting stiffness is $k_\phi = 0.36\,\mathrm{Nm/rad}$. The axial stiffness k_z can generate a sufficient force, i.e., $0.36\,\mathrm{N}$, to suspend the rotor in the z-direction with an axial deflection of $\delta z \approx 0.3\,\mathrm{mm}$. For the suspension force simulation, a sinusoidal 2-pole magneto-motive force (MMF) is imposed on the stator windings. That is, each stator winding is energized with MMF of

$$\Psi_n = \Psi_s \cos\left(\frac{\pi n}{6}\right), \tag{4}$$

where $\Psi_s = NI_s$ is the amplitude of the 2-pole suspension MMF with the winding turn-number $N = 800$ and the suspension control current I_s, and $n \in \{1, 2, \ldots, 12\}$ is the index of the phase windings. Figure 4a shows the relation between the suspension MMF amplitude Ψ_s and the suspension force toward the phase winding of $n = 12$ as computed in an ANSYS Maxwell simulation. The force/current sensitivity is computed as $K_i = 21\,\mathrm{N/A}$ in the linear range. The non-linearity out of this range is due to saturation of the stator iron.

Another set of simulations is performed to estimate the hysteresis torque. Here, a sinusoidal 6-pole MMF pattern is imposed on the stator windings. That is, each stator winding is energized with MMF of

$$\Psi_n = \Psi_r \cos\left(\frac{\pi n}{2} + \theta_e\right), \tag{5}$$

where $\Psi_r = NI_r$ is the amplitude of the 6-pole rotation MMF with the winding turn-number $N = 800$ and the rotation control current I_r, $n \in \{1, 2, \ldots, 12\}$ is the index of the

TABLE II
KEY DESIGN PARAMETERS.

	Parameter	Value
D_o	Rotor outer diameter	57 mm
D_i	Rotor inner diameter	45 mm
h	Rotor height	5 mm
m	Rotor mass	37 g
I_z	Rotor axial moment of inertia	$24.4\,\mathrm{kg \cdot mm^2}$
g_o	Outer air-gap	1 mm
g_i	Inner air-gap	2 mm
B_{bias}	Outer air-gap bias flux density	0.13 T
δz	Rotor axial sag	0.3 mm

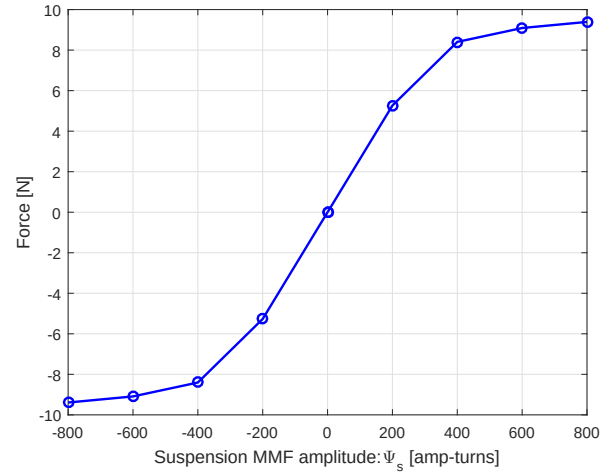

(a)

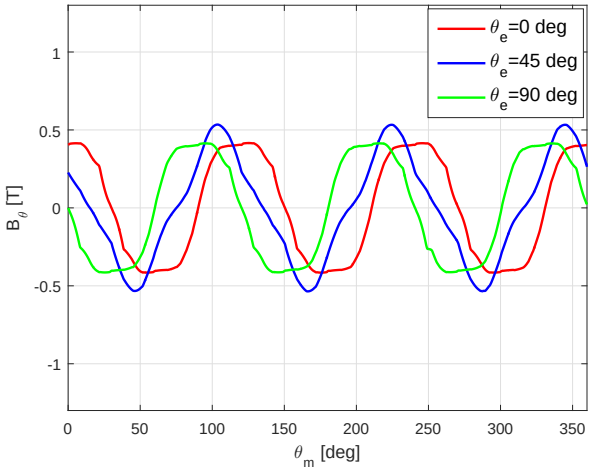

(b)

Fig. 4. FEA simulation results: (a) The relation between the suspension force and the 2-pole suspension MMF amplitude Ψ_s as computed with FEA simulations. (b) FEA simulation results showing tangential flux density distribution in the rotor induced by 6-pole rotation MMF. The electrical angle θ_e simulates a shift of the flux density as well as the MMF wave. The harmonic distortion is due to the effect of stator teeth.

TABLE III
OPEN-LOOP PERFORMANCE ESTIMATES FROM FEA SIMULATIONS.

	Parameter	Value
k_r	Radial stiffness	-5.39 N/mm
k_z	Axial stiffness	1.17 N/mm
k_ϕ	Tilting stiffness	0.36 Nm/rad
K_i	Force constant	21 N/A
τ_z	Hysteresis torque (Ψ_r = 300 amp-turns)	3.23 mNm

phase windings, and θ_e is an electrical angle. The electrical angle θ_e is the angle of traveling MMF wave. Figure 4b shows how the tangential flux density is distributed in the core of the rotor along the circumferential direction. The data in Figure 4b are computed from simulation cases where the stator is energized with six-pole traveling MMF with an amplitude of Ψ_r = 300 amp-turns and the electric angles of $\theta_e = 0°$, $45°$, and $90°$. As stated earlier, the simulation uses the normal magnetization curve which represents saturation

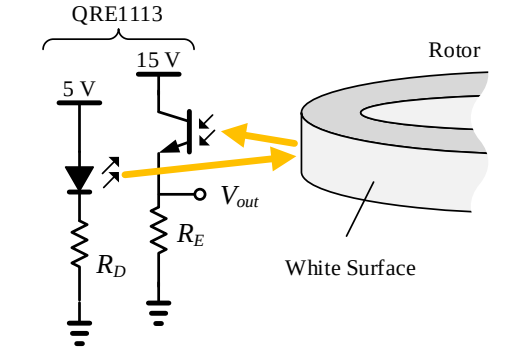

(a)

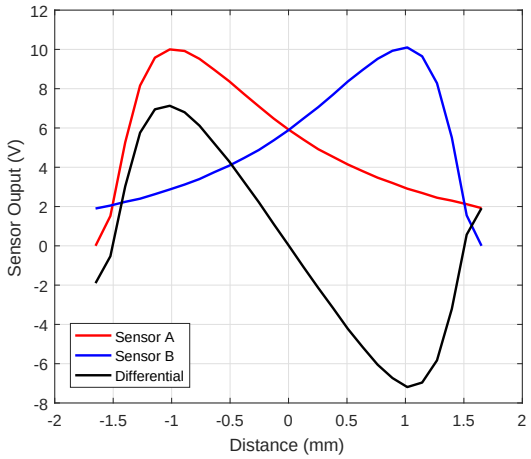

(b)

Fig. 5. Position sensing module: (a) Schematic diagram of the optical sensor (QRE1113) and the rotor. (b) Measured sensor outputs as functions of the distance to the rotor.

but not hysteresis. The resulting tangential flux densities in the rotor resemble a traveling sinusoid with an amplitude of $0.5\,\mathrm{T}$. Harmonic distortion shown in these curves is due to the effect of stator teeth.

The hysteresis torque estimate can be computed from (1) as the integral is evaluated using the experimentally measured B-H loop data shown in Figure 3. Here, the solid red line is for the case where the flux density is sinusoidal with a peak amplitude of $0.5\,\mathrm{T}$. The computed loop area is $1406\,\mathrm{A/m \cdot T}$, which leads to a hysteresis torque estimate of $\tau_z = 3.23\,\mathrm{mNm}$. The performance estimates from FEA simulations are summarized in Table III.

B. Position sensors

We use reflective-type optical sensors (QRE1113 from Fairchild Semiconductor) to measure the rotor radial positions. Each of the sensors views the rotor radially inwards through the outer air-gap, and measures the rotor radial displacement. Figure 5a shows a schematic diagram of the sensor in conjunction with the rotor. The sensor consists of an infrared LED and a phototransistor facing the same direction. With external voltage sources and resistors connected, the LED shines an infrared beam on the rotor outer surface, and the phototransistor picks up the reflected light. The rotor surface

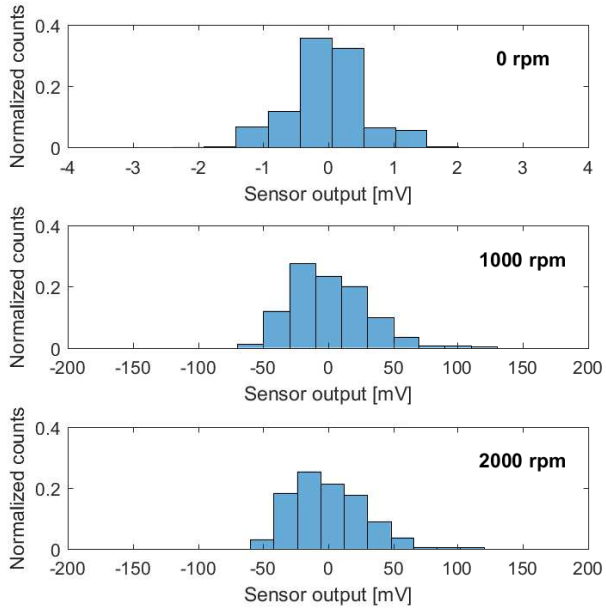

(a)

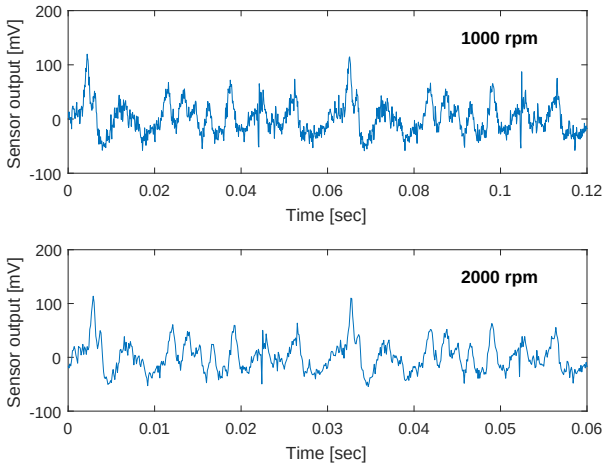

(b)

Fig. 6. Sensor noise characteristics: (a) Histrograms at various rotor speeds: 0 rpm, 1000 rpm, and 2000 rpm. (b) Sensor outputs measured at rotor speeds of 1000 rpm and 2000 rpm.

is coated with white electrical tape for better reflectivity. A current-limiting resistor of $R_D = 200\,\Omega$ is connected in series with the LED. The emitter resistor R_E is tuned such that the peak output voltage is $10\,\mathrm{V}$. As shown in Figure 7, four sensors (A through D) are inserted between the stator teeth on the two orthogonal diametric axes. One differential pair, A and B, is used to measure y-axis position, and the other differential pair, C and D, is used to measure x-axis position.

The sensor sensitivity to the distance is measured as follows: An optical sensor is mounted on a structure fixed on an optical breadboard, and the rotor is mounted on a single-axis linear micrometer stage that is fixed on the same optical breadboard. The optical sensor and the rotor are aligned so that the optical sensor's sensitive axis points at rotor's center, as illustrated in Figure 5a. The gap between the optical sensor and the rotor surface is varied from $d = 0$ to $d = 3.937\,\mathrm{mm}$ with an increment of $\Delta d = 0.127\,\mathrm{mm}$, and the sensor output is measured using an oscilloscope (Tektronix TDS2014C).

Let $e_A(d)$ and $e_B(d)$ be the outputs of sensor A and B measured as functions of distance d. In Figure 5b, the outputs of sensor A and B are plotted as $e_A(d - d_0)$ and $e_B(d_0 - d)$, where $d_0 = 1.65\,\mathrm{mm}$ is the nominal distance between the optical sensor and the rotor surface when the rotor is at the stator center. The differential measurement curve (black) is computed by taking a difference between the two: $e_A(d-d_0) - e_B(d_0 - d)$. The differential output is approximately linear in the range of $\pm 1\,\mathrm{mm}$ with a sensitivity of about $8\,\mathrm{V/mm}$.

The sensor noise characteristics are measured for various rotational speeds of the rotor. The data are acquired as follows: A separate test rig is built, on which a direct-drive DC motor (maxon DC motor RE025-055-35EBA201A) spins the rotor, and an optical sensor measures the surface of the spinning rotor. The distance between the sensor and the rotor surface is adjusted by such an amount that the nominal sensor output is about $5\,\mathrm{V}$. Then, the rotor is spun at constant rotational speeds, and the sensor outputs are acquired at a sampling rate of $10\,\mathrm{kHz}$ with a NI cRIO-9076 target equipped with an NI 9205 analog input module of $370\,\mathrm{kHz}$ bandwidth. To compensate for the error due to the mechanical eccentricity of the test rig, we subtract the fundamental frequency components from the recorded sensor outputs.

Figure 6a shows the sensor output histograms for three different rotor speeds. When the rotor is stationary, the noise standard deviation is about $0.65\,\mathrm{mV}$. As the rotor is spun, for example at 1000 rpm and 2000 rpm, the noise standard deviation increases to $\sigma = 29\,\mathrm{mV}$, which is about 45 times larger than that of the stationary case. The histograms for the rotor speeds of 1000 rpm and 2000 rpm show similar distributions. Their similarity becomes clearer when we look at the sensor outputs plotted as functions of time in Figure 6b. Here, one trace is approximately a time-scaled version of the other. We hypothesize that the fluctuation is due to the non-uniformity of the electrical tape, in terms of reflectivity and/or thickness, along the rotor circumference. As the rotor speed increases, the spectral distribution of the noise shifts to higher frequencies because the optical sensor sees relatively fast changes of the rotor surface non-uniformity.

The optical sensor is used in our prototype bearingless motor for its small size, low cost, and no interference with the stator fields. We are considering other rotor surface treatments to reduce the sensor noise.

C. Power amplifiers

Transconductance linear power amplifiers, which have been built for driving self-bearing hysteresis motors in [12] are used to drive the twelve-phase stator windings. In each amplifier board, the power stage consists of a linear power op-amp (PA12 from Apex Microtechnology), and the control stage consists of three high-voltage op-amps (OPA 445 or OPA 552 from Texas Instruments). The winding current i_{out} is measured with a sense resistor of $R_{sense} = 0.1\,\Omega$, and fed

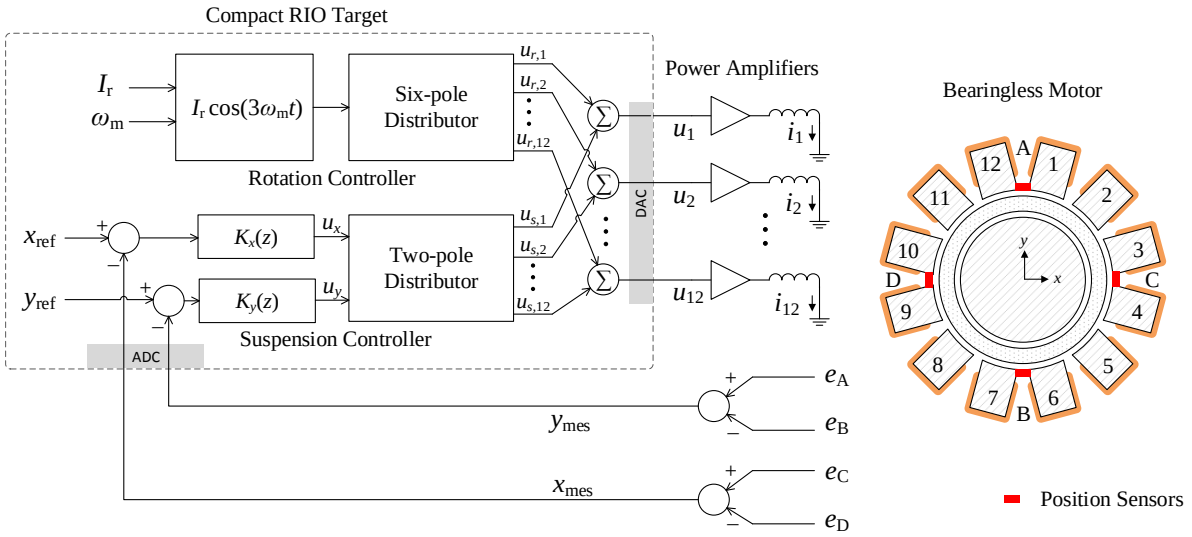

Fig. 7. Block diagram for the control system. The suspension controller forms a feedback loop with the position sensor measurements, whereas the rotation controller operates in an open-loop manner. The control signals from rotation controller and suspension controller are added and sent to twelve power amplifiers as current commands. The amplifiers drive the twelve single-phase stator windings individually.

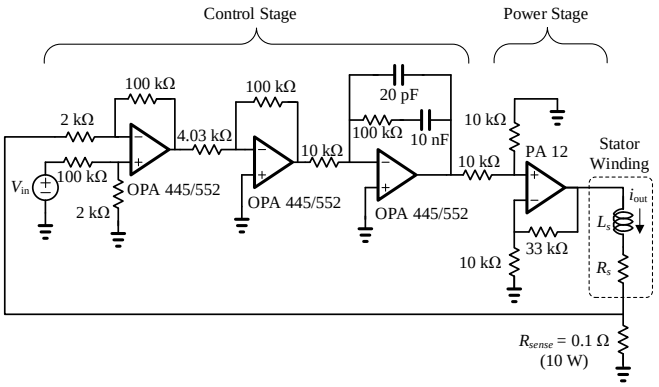

Fig. 8. Circuit schematic of the power amplifier board. The current through the stator winding is measured with a sense resistor of $R_{sense} = 0.1\,\Omega$ for feedback control. The DC transconductance is $200\,\mathrm{mA/V}$ and the loop bandwidth is about $5\,\mathrm{kHz}$ for our stator winding of $L_s = 185\,\mathrm{mH}$ and $R_s = 6\,\Omega$.

back to the control stage configured for PI compensation. All op-amps on the board share the same bus voltage, which is limited to $\pm 30\,\mathrm{V}$ by OPA 552. The power amplifiers are tuned such that the DC transconductance is $200\,\mathrm{mA/V}$ and the loop bandwidth is about $5\,\mathrm{kHz}$. The circuit schematic is shown in Figure 8. The configuration of the PA12 is stable, since the local op-amp loop return ratio has resistive feedback with an attenuation of about 4:1, which satisfies the PA12 limitations of not being unity gain stable [20].

The usage of a linear power amplifier can significantly limit the power efficiency of the whole system from the DC bus to the mechanical output port. Also, using twelve power amplifiers to individually drive twelve stator coils is not a cost-efficient implementation, given that the mechanical degrees of freedom requiring active control are only three: x, y, and θ_z. Nevertheless, the twelve linear power amplifiers are used here for the ease of testing different control algorithms in a prototyping phase.

D. Controller

As shown in Figure 7, the control algorithm consists of two sub-algorithms: the suspension controller and the rotation controller. The suspension controller forms a feedback loop with the position sensors. In contrast, the rotation controller runs in open loop. The control signals from the rotation controller $(u_{r,1}, u_{r,2}, \ldots, u_{r,12})$ are added to those from suspension controller $(u_{s,1}, u_{s,2}, \ldots, u_{s,12})$ and sent to the power amplifiers as current commands $(u_1, u_2, \ldots, u_{12})$. That is, the flux superposition happens inside the controller via addition of the current command signals. The control algorithms are implemented in an FPGA of an NI cRIO-9076 target via the LabVIEW programming language. The suspension controller runs at a loop rate of $10\,\mathrm{kHz}$, whereas the rotation controller runs at the higher loop rate of $100\,\mathrm{kHz}$.

1) Suspension controller: The two radial translations of the rotor are actively stabilized by the suspension controller. The x- and y-positions of the rotor are differentially measured with four optical sensors, i.e., $x_{mes} = e_C - e_D$ and $y_{mes} = e_A - e_B$, and fed back to the suspension controller. To achieve a loop rate of $10\,\mathrm{kHz}$, the suspension controller is implemented in the FPGA of the cRIO target. Two identical discrete-time lead controllers run in parallel for the x- and y-axes:

$$K_x(z) = K_y(z) = K_p \frac{z - b_0}{z - a_0}. \tag{6}$$

The controller parameters are set to $b_0 = 0.9391$ and $a_0 = 0.5219$, which are computed from Tustin transformation of a continuous-time lead controller with a zero at $100\,\mathrm{Hz}$ and a pole at $1\,\mathrm{kHz}$. The proportional control gain of $K_p = 7$ achieves a cross-over frequency $\omega_c = 110\,\mathrm{Hz}$ and phase margin $\phi_m = 25^\circ$ as shown in Figure 9a. The control efforts

from the lead controllers, u_x and u_y, are processed through the two-pole distributor block to generate control signals

$$u_{s,n} = u_x \sin\left(\frac{\pi n}{6} - \frac{\pi}{12}\right) + u_y \cos\left(\frac{\pi n}{6} - \frac{\pi}{12}\right), \quad (7)$$

where $n \in \{1, 2, \ldots, 12\}$ is the index of the phase windings. The angle correction of $-\pi/12$ compensates for the angle difference between the sensor axes and stator teeth. The suspension control algorithm does not require any angle-dependent transformations. This is because the suspension force generation is independent of the rotor angle as well as the angle of 6-pole rotating flux.

2) Rotation controller: Rotation about the z-axis is controlled in an open-loop manner. Given the current amplitude I_r and mechanical angular frequency ω_m, the rotation controller generates control signals

$$u_{r,n} = I_r \cos\left(\frac{\pi n}{2} + 3\omega_m t\right), \quad (8)$$

where $n \in \{1, 2, \ldots, 12\}$ is the index of the phase windings. This control law generates a 6-pole rotating MMF wave whose mechanical angular speed is ω_m and amplitude is $\Psi_r = NI_r$, where $N = 800$ is the winding turn-number. The output from the rotation controller $u_{r,n}$ is added to the output from suspension controller $u_{s,n}$ to generate the current command signals $u_n = u_{r,n} + u_{s,n}$, which are sent to the power amplifiers as current references. The signals $u_{r,n}$ may be seen as disturbances to the suspension control loop, but collectively their effects sum to zero because the 6-pole flux does not interfere with the 2-pole flux in suspension force generation as discussed in Section II-B.

IV. Performance tests

The prototype system can levitate the rotor and drive it up to 1734 rpm. Above 1734 rpm, the system exhibits instability, preventing higher speed operation. We speculate that the instability beyond this rotational speed is due to the sensor noise, whose spectral contents shift toward higher frequencies as the rotor speed increases, amplified around the cross-over frequency of the suspension control loop and pushing the rotor out of the stable operating range. The maximum driving torque is estimated as $2.67\,\mathrm{mNm}$ based on braking time measurements. This section discusses the test methods and results in more detail.

A. Suspension test

With the suspension control in operation, the rotor lifts off from the stator teeth and levitates as we gradually increase K_p in (6) from zero to about 5. We measure the frequency response of the loop return ratio to evaluate the bandwidth and stability margin of the suspension control loop. The frequency responses are measured with an HP 35665A dynamic signal analyzer from $10\,\mathrm{Hz}$ to $1\,\mathrm{kHz}$ in a frequency sweep mode. Figure 9a shows the Bode plots of the loop return ratio (blue), the controller (red), and the plant (green) for $K_p = 7$. The loop return ratio crosses through unity magnitude at $\omega_c = 110\,\mathrm{Hz}$ with a phase margin of $\phi_m = 25°$. The measured gain curves show a notch and peak around $35\,\mathrm{Hz}$, from which we can infer that the actual plant transfer function has a pair of complex zeros and poles, unexpectedly. We hypothesize that this co-located mode is due to the rotor tilting modes of second-order added to the radial mode; the amplification of tilting motion is observed around $35\,\mathrm{Hz}$ excitation during the frequency sweep measurement. Figure 9b shows the Bode plots of the loop return ratio for various K_p from 5 to 10. As K_p increases, the magnitude plots shifts up whereas the phase plots remain the same. This trend agrees with the behavior of linear time-invariant systems. Figure 9c shows the Bode plots of the loop return ratio with 6-pole MMF of various amplitude Ψ_r superimposed. Here, the proportional gain is fixed to $K_p = 10$. As Ψ_r increases, the DC gain of the loop return ratio decreases. This is because the superposition of 6-pole flux in addition to the homopolar bias flux increases the net magnitude of radial negative stiffness. This trend of increasing negative stiffness with increasing excitation MMF amplitude has been studied in [21] for the case of 4-pole biased magnetic suspension. The 6-pole flux also increases the passive tilting stiffness, which manifests itself as the resonance peak shifting to higher frequencies.

TABLE IV
Magnetic Suspension Load Capacity.

K_p	Axial Capacity (N)	Radial Capacity (N)
5	2.5	3.5
6	2.5	4.0
7	2.5	4.5
8	2.5	4.6
9	2.5	4.7
10	2.5	4.7

We measure the axial and radial load capacity of the suspension system for various K_p values, as listed in Table IV. The data are acquired as follows: The rotor is pulled vertically and horizontally via threads until the system loses stable suspension. One side of the treads is connected to the rotor, and the other side of the treads is connected to a digital force meter to measure the tension. The force meter is set to a peak detection mode, so that the maximum tension during the pulling is recorded. For axial load capacity tests, three threads are connected to the rotor side, made into a single bundle, and pulled along the positive z-axis. For radial load capacity tests, a single thread is connected to the rotor and pulled radially. The measured axial load capacity is about $2.5\,\mathrm{N}$ regardless of the K_p values, whereas the measured radial load capacity increases from $3.5\,\mathrm{N}$ to $4.7\,\mathrm{N}$ as K_p is increased from 5 to 10.

B. Rotation test

For rotation tests, the proportional gain of the suspension controller is set to $K_p = 7$. As we drive the stator with 6-pole rotating MMF, the rotor starts rotating due to the combination of hysteresis torque and induction torque. The amplitude Ψ_r and frequency ω_m of the 6-pole MMF wave are adjustable for various torques and speeds. With $\Psi_r = 160$ amp-turns and $\omega_m = 2000\,\mathrm{rpm}$, the prototype system can drive the rotor up to $\omega_m^* = 1734\,\mathrm{rpm}$ as measured with a laser tachometer. At low speeds, the rotor rotates in near synchronism with

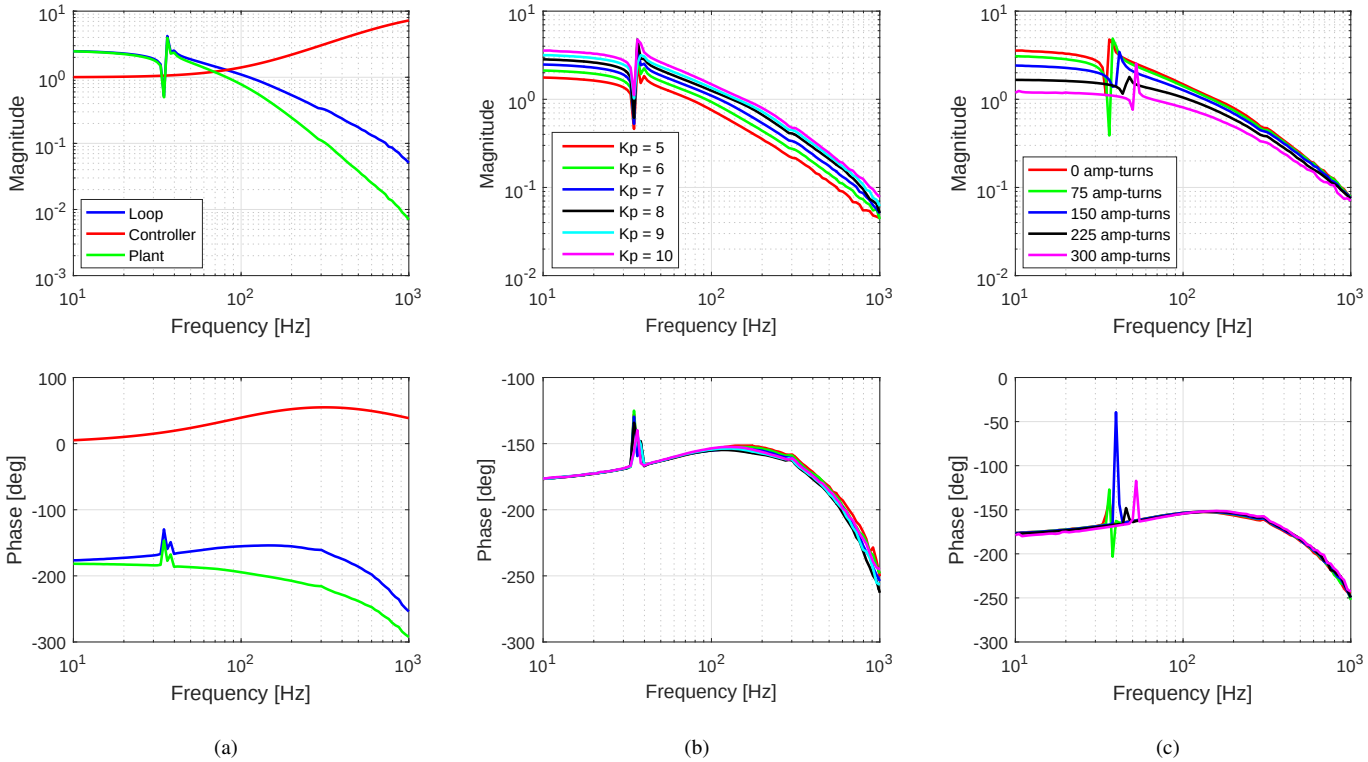

(a) (b) (c)

Fig. 9. Measured frequency responses of the suspension control system: (a) frequency responses of the loop return ratio (blue), controller (red), and plant (green) for $K_p = 7$, (b) frequency responses of the loop return ratio for various proportional gains K_p, and (c) frequency responses of the loop return ratio for various 6-pole MMF amplitudes Ψ_r for $K_p = 10$.

TABLE V
STEADY-STATE SPEEDS AND BRAKING TIMES.

Command speed (ω_m)	Measured speed (ω_m^*)	Slip (%)	Braking time (Δt_0)
200 rpm	194 rpm	3.0	4.25 s
400 rpm	383 rpm	4.2	7.05 s
600 rpm	563 rpm	6.1	9.40 s
800 rpm	754 rpm	5.8	11.70 s
1000 rpm	930 rpm	7.0	13.75 s
1200 rpm	1067 rpm	10.3	15.10 s
1400 rpm	1262 rpm	9.8	16.80 s
1600 rpm	1449 rpm	9.4	18.45 s
1800 rpm	1597 rpm	11.3	19.65 s
2000 rpm	1734 rpm	13.3	20.75 s

the 6-pole MMF wave, which is a typical characteristic of hysteresis motors. At higher speeds, however, the rotor loses synchronism due to drag torques increasing with the rotational speed. Table V shows a comparison between the command rotational speeds ω_m and the measured rotational speeds ω_m^*. The higher command speed causes a larger percentage slip, which implies that the ratio of the induction torque to the hysteresis torque increases. This is because the hysteresis motor torque is known to be constant for all slips [22, p. 462], whereas the induction torque increases proportionally to the slip at low slips. Here, the 6-pole MMF amplitude is set to Ψ_r = 160 amp-turns.

As the rotational speed is increased from zero to $1734\,\mathrm{rpm}$, the standard deviation of the rotor x-displacement sensed voltage is increased from $1\,\mathrm{mV}$ ($0.13\,\mu\mathrm{m}$) to $115\,\mathrm{mV}$ ($14.38\,\mu\mathrm{m}$). Figure 10 shows the radial vibration of the levitated rotor spinning at $1734\,\mathrm{rpm}$, as measured with the feedback optical sensors. Notice that a periodic pulse train, indicated with red circles, is embedded in the signals. This alternating pulse train

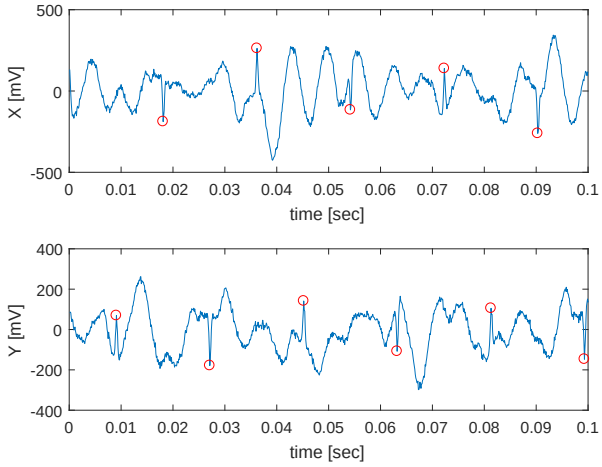

Fig. 10. Radial vibration of the rotor spinning at 1734 rpm as measured with feedback optical sensors. Red circles indicate the pulses injected when the seam of the electrical tape on the rotor passes the optical sensors. The alternating pattern is due to the differential measurement.

TABLE VI
ESTIMATION OF DRIVING TORQUES.

	Case I	Case II	Case III
Current amplitude (I_r)	100 mA	200 mA	300 mA
MMF amplitude (Ψ_r)	80 At	160 At	240 At
Command speed (ω_m)	1000 rpm	1000 rpm	1000 rpm
Measured speed (ω_m^*)	515 rpm	930 rpm	948 rpm
Braking time (Δt_1)	2.32 s	1.45 s	0.85 s
Braking torque (τ_{brake})	0.57 mNm	1.64 mNm	2.85 mNm
Driving torque (τ_{drive})	0.42 mNm	1.47 mNm	2.67 mNm

occurs when the seam of the electrical tape on the rotor passes the optical sensors. The pulse train is half-wave symmetric because of the differential measurement, and therefore its spectrum can have the odd harmonics as well as the fundamental. We speculate that as the rotor speed increases, the sensor noise spectra shift toward higher frequencies and are amplified more as they come closer to the cross-over frequency of the suspension control loop. Too much amplification of the radial vibration can push the rotor out of the stable operating range, thereby causing the observed suspension failure.

The drag torque of the magnetic suspension is estimated as follows: First, the rotor is driven with 6-pole until it reaches the steady-state speed. Then, we turn off the 6-pole MMF and measure a braking time. That is, we measure the elapsed time Δt_0 for the rotor to reach zero speed after the 6-pole MMF amplitude is set to Ψ_r = 0. The third column of Table V lists the mean braking time for each steady-state speed, from which we can estimate the mean drag torque as follows:

$$\tau_{drag} \approx \frac{I_z \Delta \omega_m^*}{\Delta t_0}. \tag{9}$$

Here, $I_z = 24.4\,\mathrm{kg \cdot mm^2}$ is the rotor axial moment of inertia.

The driving torque is estimated in a similar manner. First, we drive the rotor and wait for the steady-state. Then, we set the 6-pole MMF rotational speed to $\omega_m = 0$ and record a braking time Δt_1. The driving torque estimate is computed as follows:

$$\tau_{drive} = \tau_{brake} - \tau_{drag} \approx \frac{I_z \Delta \omega_m^*}{\Delta t_1} - \tau_{drag}. \tag{10}$$

Three cases for different MMF amplitudes are tested and the results are listed in Table VI. As the 6-pole MMF amplitude Ψ_r is increased from 160 amp-turns to 240 amp-turns, the driving torque increases from $1.47\,\mathrm{mNm}$ to $2.67\,\mathrm{mNm}$. That is, a 50% increment in amp-turns leads to a 80% torque improvement. However, higher 6-pole MMF amplitudes, for example Ψ_r = 300 amp-turns as in the simulation, lead to failure of the stable suspension with command speeds of $\omega_m = 1000\,\mathrm{rpm}$. This is because the higher 6-pole MMF amplitude decreases the low-frequency gains of the suspension loop return ratio, and therefore lowers the cross-over frequency and phase margin of the suspension control loop. Increasing K_p can recover the cross-over frequency and phase margin but at the expense of further sensor noise amplification, which prevents stable suspension as explained above.

V. CONCLUSIONS

In this paper, we have presented a new concept of bearingless motors that drives a ring-shaped hysteresis rotor. Our magnetic design combines the force generation mechanism of homopolar flux-biased magnetic bearings and the torque generation mechanism of hysteresis motors. The two mechanisms are combined in such a way that they do not interfere with each other, thereby enabling decoupled control of suspension and rotation. As a result, the suspension and rotation control does not require angle sensors and associated commutation algorithms. This characteristic, along with a simple rotor construction, is favorable for reducing the cost of the overall system. In particular, our bearingless motor shows promise in pump applications that require frequent impeller replacement, such as blood pumps.

We have built a prototype system and performed tests to evaluate the speed and torque performance. Although satisfactory as a proof of concept, the current prototype requires improvements for an application to an extra-corporeal blood pump that we aim to develop. We are currently investigating an alternative sensing scheme that can measure the rotor radial positions through a blood channel, such as eddy-current sensors. This can provide a rotor position measurement that is less sensitive to the local surface property, thereby addressing the noise issue observed in the low-cost optical sensors. To improve the torque capability, we plan to increase the thickness of the rotor, i.e., from $5\,\mathrm{mm}$ to $10\,\mathrm{mm}$, to enlarge the traction surface area, thereby increasing the torque for the same air-gap shear stress. This also increases the inertia of the levitated body, which can reduce the unstable pole frequency for the same negative stiffness and make the suspension control easier. Also, larger inertia can improve the dynamic stiffness at high frequencies [23, P. 67]. Utilizing a more magnetically-hard material, such as Alnico, can further increase the torque capability within the same rotor volume. We also plan to design a new winding scheme consisting of two separate sets, one for suspension and the other for rotation. In each winding set, multiple coils can be connected in series to form phases of less number, i.e., two or three phases, so as to reduce the number of power amplifiers required.

ACKNOWLEDGMENT

Research reported in this publication was supported by the National Heart, Lung, And Blood Institute of the National Institutes of Health under Award Number R41HL134455. The content is solely the responsibility of the authors and does not necessarily represent the official views of the National Institutes of Health.

The authors thank the Samsung Scholarship for partially funding the first author's graduate program, and thank National Instruments for donation of the controller hardware used in this research.

REFERENCES

[1] A. Chiba, T. Fukao, O. Ichikawa, M. Oshima, M. Takemoto, and D. G. Dorrell, *Magnetic Bearings and Bearingless Drives*. Elsevier, 2005.

[2] N. Barletta and R. Schöb, "Design of a bearingless blood pump," in *Proc. 3rd International Symposium on Magnetic Suspension Technology*, Jul. 1996, pp. 265–274, part 1.

[3] S. Ueno, C. Chen, T. Ohishi, K. Matsuda, Y. Okada, Y. Taenaka, and T. Masuzawa, "Design of a self-bearing slice motor for a centrifugal blood pump," in *Proc. 6th International Symposium on Magnetic Bearings*, Aug. 1998, pp. 143–151.

[4] R. Schöb, N. Barletta, A. Fleischli, G. Foiera, T. Gempp, H.-G. Reiter, V. L. Poirier, D. B. Gernes, K. Bourque, H. M. Loree, and J. S. Richardson, "A bearingless motor for a left ventricular assist device (LVAD)," in *Proc. 7th International Symposium on Magnetic Bearings*, Aug. 2000, pp. 383–388.

[5] H. Onuma, T. Masuzawa, K. Matsuda, and Y. Okada, "Magnetically levitated centrifugal blood pump with radially suspended self-bearing motor," in *Proc. 8th International Symposium on Magnetic Bearings*, Aug. 2002, pp. 3–8.

[6] J. Asama, T. Shinshi, H. Hoshi, S. Takatani, and A. Shimokohbe, "A compact highly efficient and low hemolytic centrifugal blood pump with a magnetically levitated impeller," *Artificial Organs*, vol. 30, no. 3, pp. 160–167, Mar. 2006.

[7] J. Asama, T. Fukao, A. Chiba, A. Rahman, and T. Oiwa, "A design consideration of a novel bearingless disk motor for artificial hearts," in *Proc. 2009 IEEE Energy Conversion Congress and Exposition*, Sep. 2009, pp. 1693–1699.

[8] H. Onuma and T. Masuzawa, "Evaluation of magnetic suspension characteristics and levitation performance of a centrifugal blood pump using radial type self-bearing motor," in *Proc. 14th International Symposium on Magnetic Bearings*, Aug. 2014, pp. 174–179.

[9] R. Schöb and N. Barletta, "Principle and application of a bearingless slice motor," in *Proc. 5th International Symposium on Magnetic Bearings*, Aug. 1996, pp. 313–318.

[10] S. Silber, W. Amrhein, P. Bösch, R. Schöb, and N. Barletta, "Design aspects of bearingless slice motors," *IEEE/ASME Transactions on Mechatronics*, vol. 10, no. 6, pp. 611–617, Dec. 2005.

[11] W. Gruber, M. Rothböck, and R. Schöb, "Design of a novel homopolar bearingless slice motor with reluctance rotor," *IEEE Transactions on Industry Applications*, vol. 51, no. 2, pp. 1456–1464, Mar. 2015.

[12] M. Imani Nejad, "Self-bearing motor design & control," Ph.D. dissertation, Mechanical Eng. Dept., Massachusetts Institute of Technology, Cambridge, MA, USA, Feb. 2013.

[13] L. Zhou, "Magnetically suspended reaction sphere with one-axis hysteresis drive," Master's thesis, Mechanical Eng. Dept., Massachusetts Institute of Technology, Cambridge, MA, USA, Jun. 2014.

[14] P. A. Studer, "A practical magnetic bearing," *IEEE Transactions on Magnetics*, vol. 13, no. 5, pp. 1155–1157, Sep. 1977.

[15] P. E. Allaire, E. H. Maslen, R. R. Humphris, C. K. Sortore, and P. A. Studer, "Low power magnetic bearing design for high speed rotating machinery," in *Proc. International Symposium on Magnetic Suspension Technology*, May 1992, pp. 317–329, part 1.

[16] O. Ichikawa, A. Chiba, and T. Fukao, "Inherently decoupled magnetic suspension in homopolar-type bearingless motors," *IEEE Transactions on Industry Applications*, vol. 37, no. 6, pp. 1668–1674, Nov. 2001.

[17] M. Noh, W. Gruber, and D. L. Trumper, "Homopolar-biased hysteresis bearingless slice motors," in *Proc. 15th International Symposium on Magnetic Bearings*, Aug. 2016.

[18] M. Noh and D. L. Trumper, "Homopolar, flux-biased hysteresis bearingless motor," U.S. Patent Application 20170040868, Feb 2017.

[19] B. R. Teare, "Theory of hysteresis-motor torque," *AIEE Transactions*, vol. 59, no. 12, pp. 907–912, Dec. 1940.

[20] *PA12·PA12A Power Operational Amplifier*, PA12U REVV, Apex Microtechnology, 2012. [Online]. Available: https://www.apexanalog.com/resources/products/pa12u.pdf

[21] L. Zhou and D. L. Trumper, "Reluctance force magnetic suspension characteristics and control for cylindrical rotor bearingless motors," *Journal of Dynamic Systems, Measurement, and Control*, vol. 139, no. 3, p. 031003, 2017.

[22] A. Fitzgerald, J. Charles Kingsley, and S. D. Imans, *Electric Machinery*. McGraw-Hill, 2003.

[23] H. Bleuler, M. Cole, P. Keogh, R. Larsonneur, E. Maslen, R. Nordmann, Y. Okada, G. Schweitzer, and A. Traxler, *Magnetic Bearings*, G. Schweitzer and E. Maslen, Eds. Springer-Verlag, 2009.

Minkyun Noh received the B.S. degree in Mechanical and Aerospace Engineering from Seoul National University, Seoul, Korea, in 2012, and the S.M. degree in Mechanical Engineering from the Massachusetts Institute of Technology (MIT), Cambridge, in 2014. He is currently a Ph.D. candidate in the MIT Department of Mechanical Engineering.

His research interests are in the design and control of mechatronic systems, with a focus on electromagnetic sensors and actuators, precision machines, and medical devices.

Wolfgang Gruber received the Dipl.-Ing. (M.S.) degree in Mechatronics and Dr. techn. (Ph.D.) degree in Technical Sciences from Johannes Kepler University, Linz, Austria, in 2004 and 2009, respectively. Since 2004 he has been Scientific and Research Assistant at the Institute of Electrical Drives and Power Electronics at the Johannes Kepler University Linz (JKU) and Senior Researcher at the Linz Center of Mechatronics GmbH (LCM), where he has been involved in teaching and various industrial research projects. Since 2012 he holds the rank Assistant Professor. His research has focused on new topologies for bearingless slice motors, their design, setup and, control. He is a member of the IEEE.

David L. Trumper joined the MIT Department of Mechanical Engineering in August 1993, and holds the rank of Professor. He received the B.S., M.S., and Ph.D. degrees from MIT in Electrical Engineering and Computer Science, in 1980, 1984, and 1990, respectively. Following the Bachelor's degree, Professor Trumper worked two years for the Hewlett-Packard Co. After finishing the Master's degree, he worked for two years for the Waters Chromatography Division of Millipore. Upon completing the Ph.D. degree, for three years he was an Assistant Professor in the Electrical Engineering Department at the University of North Carolina at Charlotte, working within the precision engineering group.

Professor Trumper's research centers on the design of precision mechatronic systems, with a focus on the design of novel mechanisms, actuators, sensors, and control systems. He has conducted research in topics including precision motion control, high-performance manufacturing equipment, novel measurement instruments, biomedical and bioinstrumentation devices, and high-precision magnetic suspensions and bearings. He is a member of the IEEE, ASME, and ASPE (past-President).